small methods
www.small-methods.com

Synergistic Passivation With Phenylpropylammonium Bromide for Efficient Inverted Perovskite Solar Cells

Annan Zhu, Hao Gu, Wang Li, Jinfeng Liao, Junmin Xia, Chao Liang, Guoxing Sun, Zhendong Sha, and Guichuan Xing**

Inverted perovskite solar cells (PSCs) are a promising technology for commercialization due to their reliable operation and scalable fabrication. However, in inverted PSCs, depositing a high-quality perovskite layer comparable to those realized in normal structures still presents some challenges. Defects at grain boundaries and interfaces between the active layer and carrier extraction layer seriously hinder the power conversion efficiency (PCE) and stability of these cells. In this work, it is shown that synergistic bulk doping and surface treatment of triple-cation mixed-halide perovskites with phenylpropylammonium bromine (PPABr) can improve the efficiency and stability of inverted PSCs. The PPABr ligand is effective in eliminating halide vacancy defects and uncoordinated Pb^{2+} ions at both grain boundaries and interfaces. In addition, a 2D Ruddlesden–Popper (2D-RP) perovskite capping layer is formed on the surface of 3D perovskite by using PPABr post-treatment. This 2D-RP perovskite capping layer possesses a concentrated phase distribution $\approx n = 2$. This capping layer not only reduces interfacial non-radiative recombination loss and improves carrier extraction ability but also promotes stability and efficiency. As a result, the inverted PSCs achieve a champion PCE of over 23%, with an open-circuit voltage as high as 1.15 V and a fill factor of over 83%.

1. Introduction

Perovskite solar cells (PSCs) have attracted significant attention as an efficient photovoltaic technology due to their superior optoelectronic properties, such as long charge carrier diffusion length, balanced carrier mobility, and tunable bandgap.[1] They can be manufactured with low cost technologies, including spin coating, dip coating, metal evaporation, and inkjet printing.[2–4] Over the last 15 years, the latest best research-cell power conversion efficiency (PCE) of PSCs has been rapidly increased to 26%, approaching that of single crystal silicon solar cells.[5–9] This impressive performance combined with their low cost and reliable operational stability makes PSCs a promising option for commercial applications.[10–12] In view of the PSCs' structures, the inverted (p–i–n) PSCs have been investigated as a promising photovoltaics alternative owing to their reduced hysteresis effect, easily scalable fabrication process, durable operation, and compatibility with flexible wearable optoelectronic devices.[13–15]

Despite these advantages of inverted-PSCs, depositing a high-quality perovskite layer that is comparable to those realized in normal structures still presents some challenges. Their performance is hampered by non-radiative recombination losses arising from various types of defects. These defects can act as a pathway for moisture to permeate into the perovskite layer, causing ion migration and degradation of the perovskite light-harvesting layer lattice. In addition, the presence of bulk defects and interface defects between the perovskite layer and the charge carrier extraction layer can lead to limited charge carrier extraction, energy level alignment mismatch, and photovoltaic instability, resulting in open-circuit voltage (V_{OC}) deficits, low fill factor (FF), and reduced power conversion efficiency (PCE).[16,17] To overcome these challenges and enhance the stability of perovskites, various passivation additives have been developed to facilitate the crystallization of perovskite films, restore grain boundaries, and tailor energy level alignment.[18–21] Among these, phenyl-ammonium halide salts have been widely employed for bulk passivation or surface modification of PSCs due to the strong interaction between NH_3^+ of the ligand and surface ions, which can eliminate halide and organic cation vacancies.[22–26] However, the synergistic passivation effect of bulk and interface engineering by phenylpropylammonium halide remains unclear.[27–32]

In this work, we introduce phenylpropylammonium bromine (PPABr) as a bulk and interface passivation additive into triple-cation mixed-halide precursors and post-treat it onto 3D

A. Zhu, H. Gu, W. Li, J. Liao, J. Xia, C. Liang, G. Sun, G. Xing
Joint Key Laboratory of the Ministry of Education
Institute of Applied Physics and Materials Engineering
University of Macau
Avenida da Universidade
Taipa, Macau 999078, P. R. China
E-mail: gcxing@um.edu.mo

Z. Sha
State Key Laboratory for Strength and Vibration of Mechanical Structures
School of Aerospace Engineering
Xi'an Jiaotong University
Xi'an 710049, P. R. China
E-mail: zhendongsha@mail.xjtu.edu.cn

The ORCID identification number(s) for the author(s) of this article can be found under https://doi.org/10.1002/smtd.202300428

DOI: 10.1002/smtd.202300428

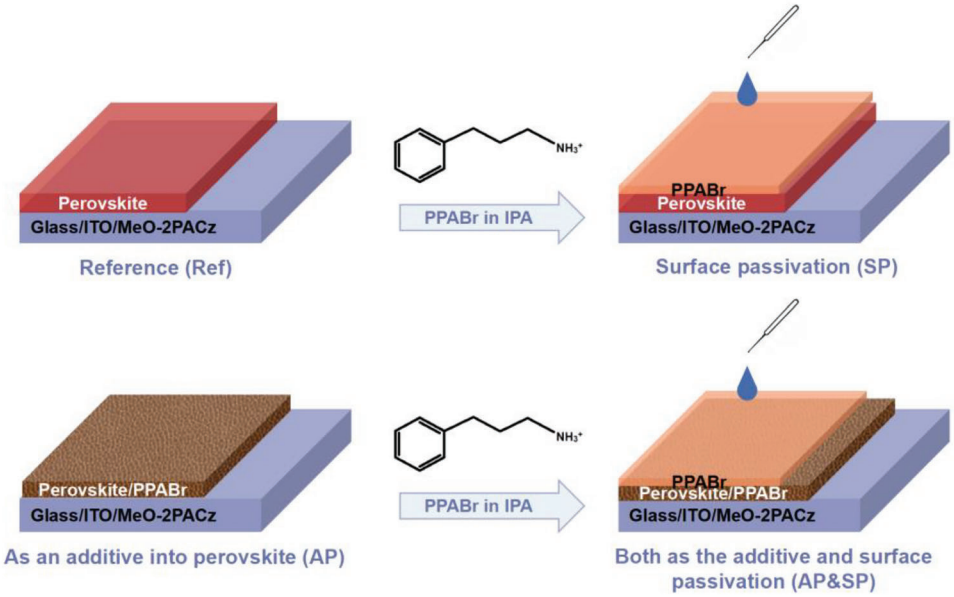

Figure 1. Schematic illustration of the fabrication of four different perovskite specimens.

perovskite top surfaces for improving the efficiency and stability of inverted PSCs. The PPABr ligand effectively eliminates halide vacancy defects and uncoordinated Pb^{2+} ions at both grain boundaries and interfaces. Furthermore, a 2D-RP perovskite capping layer with a concentrated phase distribution $\approx n = 2$ is created on the surface of the 3D perovskite. This not only tailors the energy level alignment between the 3D perovskite and the electron transport layer (ETL) but also reduces interfacial recombination loss and improves carrier extraction efficiency. Moreover, the alternative arrangement of organic and inorganic layers can provide protection against degradation and hinder ion migration of halide under long-term operation conditions, thereby forming stable PSCs. Our approach leads to the highest PCE of over 23% for the inverted PSCs, with a V_{OC} of 1.15 V and a fill factor of over 83%. The introduction of PPABr as a synergistic bulk doping and surface treatment additive with the formation of 2D-RP perovskite capping layer is proved to be effective in enhancing the performance of inverted PSCs.

2. Results and Discussion

In our experiment, four different perovskite specimens are prepared as illustrated in **Figure 1**: pure perovskite specimen without any modification, perovskite specimen with additives, perovskite specimen with surface passivation, and perovskite specimen with the additives and surface passivation, which are hereafter referred to as the "Ref," "AP," "SP," and "AP&SP," respectively. 0.5 mg mL^{-1} PPABr in perovskite solution is used in AP, and 1.0 mg mL^{-1} solution in isopropanol spinning onto perovskite films is used in SP. It is noted that the AP&SP specimen are incorporated with the part of AP and SP, without any other operations. The PSCs structures of different treatments are shown in Figure S1, Supporting Information.

To pin down the effects of PPABr on the perovskite films, we analyze the morphology and crystal structure. The scanning electron microscopy (SEM) images of the film morphology for pure perovskite, AP, SP, and AP&SP, are shown in **Figure 2**a. The grain size of SP film is almost unchanged compared to pure perovskite. Meanwhile, white impurities are found at grain boundaries because excessive PbI_2 agglomerates and deposits exist on the surface of perovskite. The grain size of perovskite film with additives becomes larger in comparison with the pure perovskite and surface passivation specimen (Figure S2, Supporting Information). The white crystals mentioned above can be identified as excessive PbI_2, and their quantity significantly decreases after additives treatment. Moreover, in view of the brightness of the picture, we observe some improvement in the overall conductivity, which may be the reason for the improved efficiency of PSCs after treatment. This result motivates us to look further into the film surface morphology via atomic force microscope (AFM). As shown in Figure 2b, obvious improvements in perovskite surface are observed. After additives treatment, the root-mean-square (R_q) value of the surface roughness decreases from 18.1 nm to 15.2 nm. This decrease behavior indicates that PPABr added to the perovskite precursor solution can passivate the grain boundaries to a certain extent during the perovskite film formation. Moreover, the surface treatment has a more significant impact, resulting in a 5 nm R_q reduction in surface roughness. PPABr at the interface causes recrystallization of perovskite; and hence, 2D perovskite films formed at the interface have smoother surfaces compared with the 3D bulk perovskite.[33] The evidence of 2D perovskite formation can be found in X-ray photoelectron spectroscopy N 1s spectra and transient absorption spectra. These results show that the passivation by PPABr for perovskite films and a uniform coverage formed at the surface of perovskite may lift the charge extraction efficiency and humidity stability.

Figure 2c depicts the changes in the wettability of the perovskite surfaces. All the figures are captured at 10 s after dropping water on the perovskite surface. The contact angle of water on the pure perovskite film is 42.1°, which increases

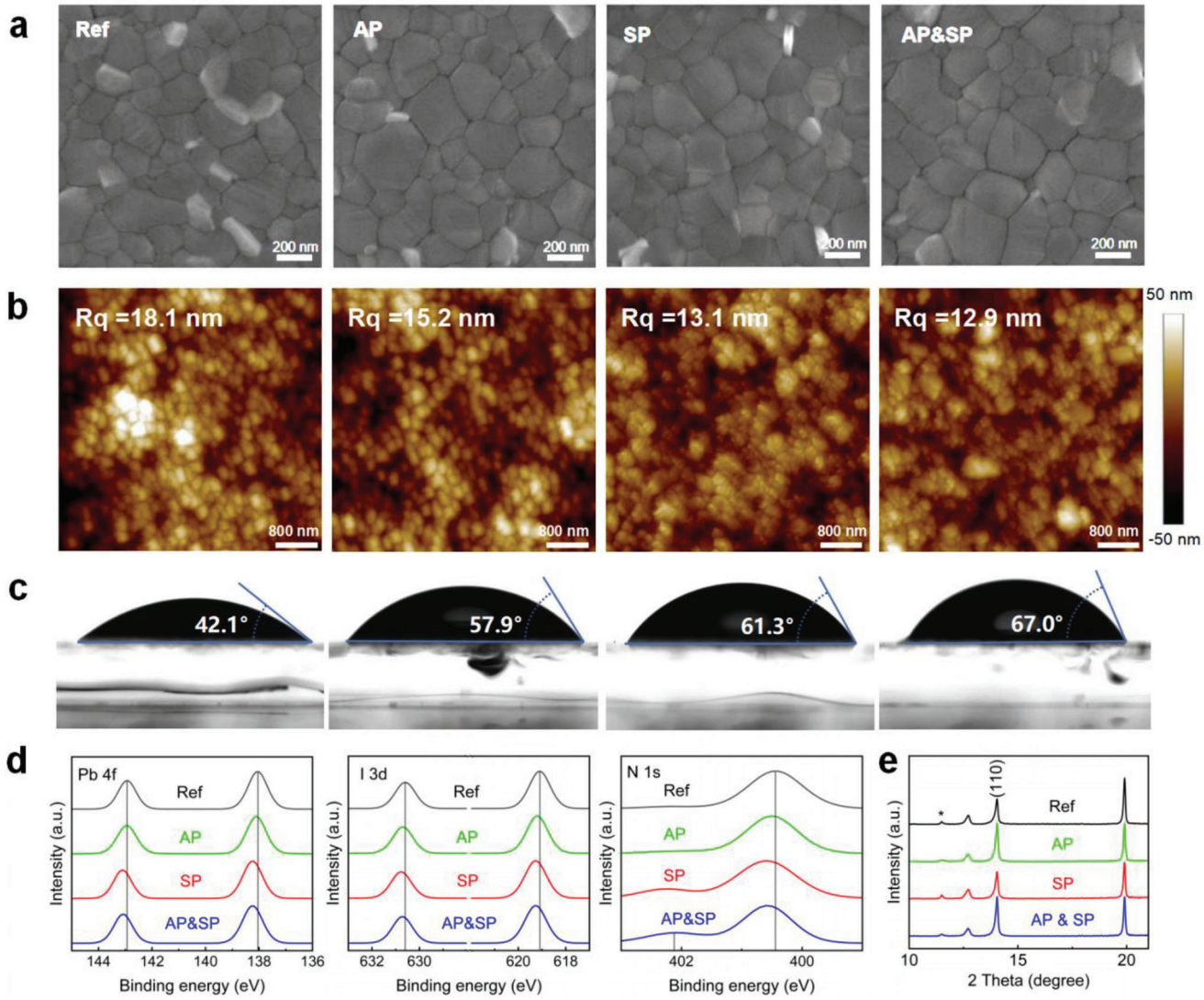

Figure 2. Surface properties of perovskite films of Ref, AP, SP, and AP&SP specimens. a) SEM images. b) AFM images. c) Contact angles. The figures were captured at 10 s after dropping water on the perovskite surfaces. d) Binding energy of Pb 4f, I 3d, and N 1s by high-resolution XPS core-level spectra. e) XRD images.

dramatically to 57.9°, 61.3°, and 67.0° for the AP, SP, and AP&SP specimens, respectively. The increase of contact angle suggests an improved water and moisture resistance, which is possibly caused by the hydrophobic benzene rings in PPABr and the passivation of surface defects to prevent hydration and decomposition reactions.[34,35] Better humidity stability is finally obtained.

In order to study the effect of PPABr on the elemental binding energy for the four different perovskite specimens, we examine the molecular interactions by means of X-ray photoelectron spectroscopy (XPS). As shown in Figure 2d, the AP and SP specimens have a valid surface modification in perovskite. The two peaks positioned at 142.9 and 138.0 eV are both assigned to Pb^{2+}. Although the two peaks are almost unchanged for the AP specimen, they shift by 0.2 eV for the SP specimen. This shift is caused by the formation of 2D perovskite, which enhances the interaction between ligand molecules and Pb^{2+} ions. A similar phenomenon is observed in the peak of Br 3d (Figure S3, Supporting Information). However, Br atoms exist not only in perovskite but also as part of the molecule in PPABr due to incomplete dissolution and reaction. I 3d spectrum shows a more convincing shift of binding energies for the additives and surface passivation treatments due to the hydrogen interaction, indicating the enhanced interaction on the perovskite surface. The main peak of N 1s shows a similar shift compared with Pb 4f and I 3d, while a new peak occurs after surface passivation treatment. We consider the main peak located around 400.4 eV to be $C{=}NH_2^+$ in formamidinium of perovskite solution, and the new peak after surface passivation treatment around 402.1 eV to be $C{-}NH_3^+$. $C{-}NH_3^+$ exists in methylammonium introduced by perovskite solution. Nevertheless, it remains undercover in pure perovskite and AP specimens. Thus, the signals of $C{-}NH_3^+$ are assigned to PPABr introduced by the 2D perovskite component formed after surface passivation treatment. The combined XPS spectra elucidate the passivation

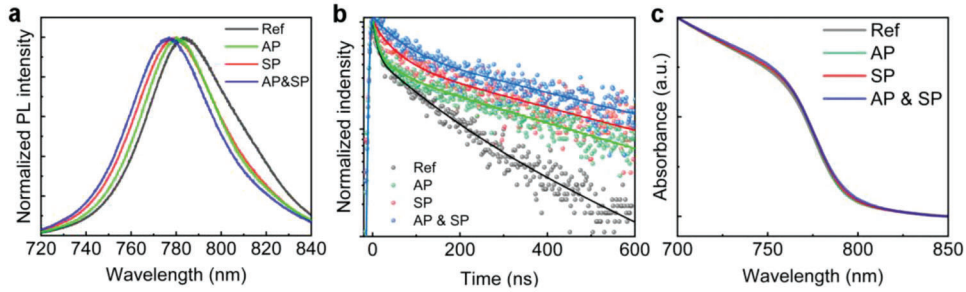

Figure 3. Steady state and time-resolved photoluminescence properties of the Ref, AP, SP, and AP&SP specimens. a) PL spectra. b) TRPL spectra upon 400 nm (100 fs, 1 kHz, ≈0.06 μJ cm^{-2}) laser pulses excitation. c) Absorbance spectra.

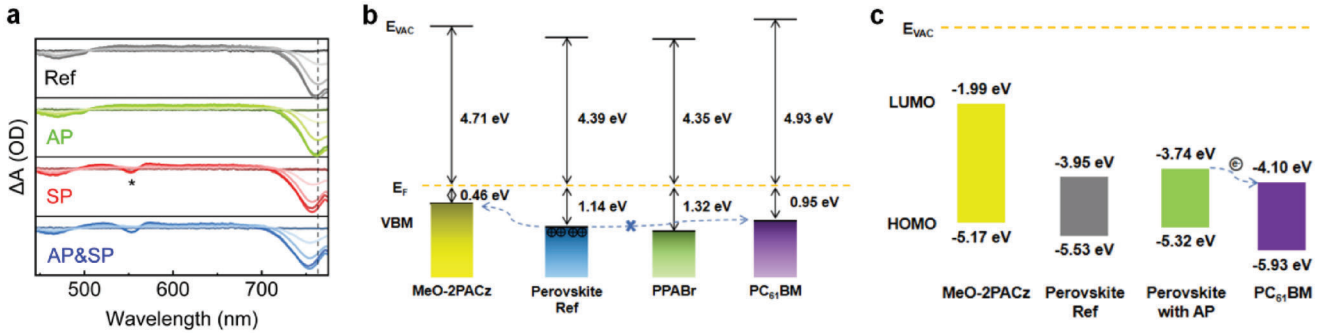

Figure 4. a) Transient absorption spectra. The Δ*A* spectra were collected at selected probe delay times of −5 ps, 1 ps, 3 ps, 1 ns, and 7.8 ns following excitation at 400 nm (100 fs, 1 kHz, ≈1.0 μJ cm^{-2}). b) Band edge positions of functional layers extracted from UPS measurements. E_{VAC} is the vacuum level, E_F is the Fermi level, and VBM is the valence band maximum. "MeO-2PACz" is glass/ITO/MeO-2PACz. "Perovskite Ref" is glass/ITO/MeO-2PACz/Perovskite Ref. "PPABr" is glass/ITO/MeO-2PACz/Perovskite Ref/PPABr. "$PCB_{61}M$" is glass/ITO/MeO-2PACz/Perovskite Ref/PPABr/$PCB_{61}M$. c) Energetic alignment of functional layers extracted from UPS measurements. Band gap widths for the surfaces of MeO-2PACz and $PCB_{61}M$ are taken from previous work.[39,40] HOMO is the highest occupied molecular orbital and LUMO is the lowest unoccupied molecular orbital.

mechanisms and provide insights on the chemical composition near the surface of perovskites.

From the X-ray diffraction (XRD) in Figure 2e, by comparing the intensities of perovskite diffraction peaks at (110), it is seen that the additives specimens can significantly increase the peak intensities of perovskite films, indicating that PPABr-doped perovskite has better isotropy. Besides, the characteristic peak of non-perovskite phase (*) is suppressed from the XRD pattern of the film with AP and AP&SP specimens.

The above findings highlight that both the additives and surface passivation treatments can passivate the perovskite surface. Previous studies showed that surface defects would produce red shift photoluminescence (PL).[36] In our work, the PL spectrum in **Figure 3**a indicates that the emission of pure perovskite films is located at 784 nm. In addition, compared with pure PSC specimen, the AP and SP specimens give rise to blue shifts of 5 and 6 nm, respectively. Moreover, an apparent blue shift of 9 nm is observed for the AP&SP specimen. These blue shifts provide direct evidence of defect passivation. We perform time-resolved photoluminescence (TRPL, excited at 400 nm on the perovskite side) measurements based on the same condition to make a further affirmation (Figure 3b). It is found out that the average carrier lifetime of the pure perovskite is 152.60 ns, which is great, shorter than the treated perovskite (314.61, 354.36, and 385.55 ns for AP, SP, and AP&SP specimens, respectively). Key TRPL parameters are listed in Table S1, Supporting Information. Nonradiative recombination centers in bulk and surface are found to be suppressed for both AP and SP specimens due to the extended carrier lifetimes. An improved V_{OC} is expected in PSCs with the suppressed nonradiative recombination, which will be confirmed by the *J–V* characteristics discussed below. Photographs and absorption spectra of perovskite films are shown in Figure 3c. The films exhibit an unchanged absorption profile, indicating that the involvement of PPABr has no effect on the light absorption capacity and band gap of perovskite (Figure S4, Supporting Information).

From the transient absorption (TA) spectra of the perovskite films (**Figure 4**a), we can clearly see that the band edge photobleaching (PB) peak exhibits a slight blue shift with the additives. The perovskite films for TA measurements were deposited with 1/3 of the initial precursor concentration, and PPABr in AP and SP specimens was added by 2.0 mg mL^{-1} to show a noticeable change. The PB peak at the position of 553 nm for the SP specimen indicates the presence of 2D perovskite ($n = 2$) within the deposited film.[37] This could be the reason for R_q reduction, contact angle improvement, and the significant shift of binding energies. A thin layer of 2D perovskite is more beneficial to the PCE promotion of PSCs because electrons will spontaneously travel from the 3D bulk to the 2D perovskite surface. The kinetics in Figure S5, Supporting Information, indicate the efficient exciton transport between the $n = 2$ layer and the 3D perovskite layer. For both 3D and 2D perovskites, after 10 ps of excitation, the AP&SP specimen showed a slower decrease in carrier kinetics compared

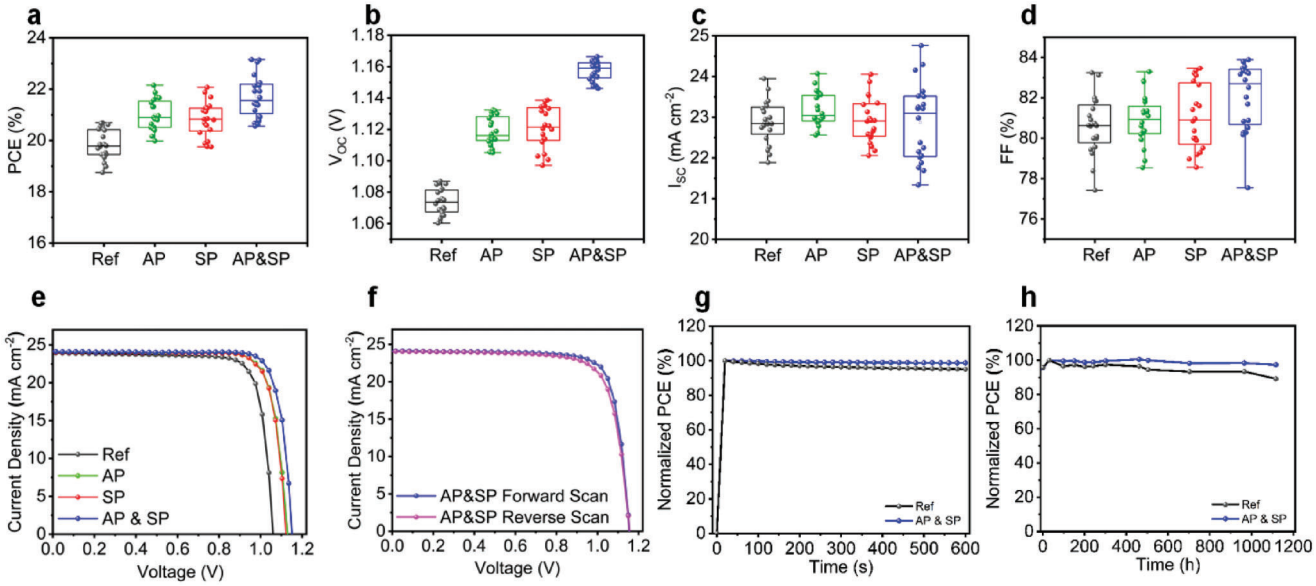

Figure 5. Performance of PSCs for Ref, AP, SP, and AP&SP specimens. Statistical photovoltaic parameters, including a) PCE, b) V_{OC}, c) J_{SC}, and d) FF diagram. e) *J–V* curves. f) Forward scan (FS, −0.05 to 1.25 V) and reverse scan (RS, 1.25 to −0.05 V) for the AP&SP device. Normalized PCE of Ref and AP&SP specimens as a function of g) illumination time during 10 min of continuous operation and h) storage time in the glove box without encapsulation.

with the SP specimen, indicating that the additives treatment is a more effective perovskite surface passivation method; and hence, associated with a longer decay time.

Ultraviolet photoelectron spectroscopy (UPS) measurements are performed to assess the HTL/perovskite/ETL transport process of our films (Figures S6 and S7, Supporting Information). The band edge positions are derived, and all values are referenced to the Fermi level, as shown in Figure 4b; Figure S6, Supporting Information.[38] The MeO-2PACz layer and PCBM upon the perovskite layer have valence band maximums similar to the previous work, which are −5.17 and −5.93 eV, respectively.[39,40] On the other hand, the Fermi level uplifts from −4.39 to −4.12 eV, and the valence band is almost unchanged for the AP specimen, implying that the perovskite becomes more n-type due to the reduced electron trap density (Figure S8, Supporting Information). In contrast to the AP specimen, the SP specimen exhibits a deeper valence band edge with a lower valence band and a higher Fermi level, inducing a deeper valence band edge caused by the formation of the 2D-perovskite phase. It is known that the electronic properties of the 2D-perovskite surface layer are different from the 3D bulk perovskite, which is expected to provide a thin surface blocking hole transport between perovskite and $PC_{61}BM$. This is more beneficial for the suppression of interfacial recombination and the enhancement of the voltage of PSCs. Besides, the ultrathin surface allows electrons to travel; and thus, remains a high current in solar cells. However, when the concentration of PPABr is further increased in the AP specimen, it can lead to a decrease in current density and FF. This is because the thick capping layer created by the high concentration of PPABr can block the extraction of electrons and affect the photogenerated carrier collection efficiency.[41]

The diagrams for the energy level alignment of functional layers (Figure 4c; Figure S9, Supporting Information) indicate the electron transport properties. For perovskite films, the band gap E_g of 1.58 eV is calculated from the Tauc plot (Figure S4, Supporting Information), remaining almost unchanged in the AP and SP specimens. The E_g values for the surfaces of MeO-2PACz and $PCB_{61}M$ are obtained from the literature,[39,40] and all values are referenced to the vacuum level. For AP specimen, a shallower energy level and a bigger energy offset between the perovskite conduction band edge and the lowest unoccupied molecular orbital level of the $PC_{61}BM$ result in smoother conduction of electrons. Our findings reveal that the AP&SP specimen shows a better performance compared with the pure perovskite specimen.

The photovoltaic characteristics of the four PSC specimens are shown in **Figure 5**a–e. Some extracted cell parameters are listed in **Table 1**. The V_{OC} values of pure PSC, AP, SP, and AP&SP specimen are 1.06, 1.13, 1.12, and 1.15 eV, respectively. Compared with pure PSCs, additives treatment and surface passivation treatment can significantly increase the V_{OC}. Moreover, the short-circuit current (J_{SC}), together with the FF, is also slightly improved because of lower defect density and more suitable energy level alignment. Through the two-step process of AP and SP treatments, AP&SP PSCs achieve a high V_{OC} of 1.15 V and FF above 83%, which are much higher than those of pure PSCs (1.06 V, 80.87%). After optimization, the PSC based on AP&SP film delivers a PCE of 23.15%, compared to 20.55% of pure PSC with negligible hysteresis (Figure 5f), and an aperture area of 0.05 cm^2. It has been found out that the concentration of PPABr is of great importance for the device performance. The optimized concentration is 0.5 mg mL^{-1} in the AP specimen and 1.0 mg mL^{-1} in the SP specimen. The J_{SC} and PCE will decrease significantly with the increase of the concentration (Figure S10, Supporting Information), which is mainly attributed to the formation of thin 2D interface which forms a barrier layer on the perovskite surface and blocks the transfer of electrons. In addition to the PCE, the stability of the

Table 1. Key photovoltaic parameters for Ref, AP, SP, and AP&SP specimens.

	V_{OC} [V]	J_{SC} [mA cm^{-2}]	FF [%]	PCE [%]
Ref	1.06	23.97	80.87	20.55
AP	1.13	24.09	81.31	22.15
SP	1.12	24.08	81.65	22.07
AP&SP	1.15	24.18	83.13	23.15

PSC device is also essential for practical application. Therefore, the stability of the devices is examined (Figure 5g,h), suggesting improved stability for PSC specimen after the additives and surface passivation treatment. The pure PSC specimen exhibits a degradation of 10% after storage without encapsulation for 1117 h. In contrast, after the additives and surface passivation treatment, the device maintains 97% of the original PCE. This result is consistent with the above observed film humidity stability and passivation improvement.

3. Conclusion

PPABr is an effective molecule in perovskite solution and at the perovskite–ETL interface. Both additives and surface passivation treatments can significantly increase the V_{OC} of PSCs due to the effective passivation of the grain boundaries, the bulk surface, and the formation of a 2D perovskite layer, resulting in an improved water and moisture resistance and enhanced bonding energy on the perovskite surface. Nonradiative recombination centers in the perovskite bulk and interfacial recombination between perovskite and ETL are reduced. By tuning the concentration of PPABr, high PCE of inverted PSCs up to 23.15% is achieved. Concurrently, the device show no dramatic PCE decay even when stored without any encapsulation. Our study provides insight into the synergistic passivation that can effectively obtain high efficiency inverted PSCs.

4. Experimental Section

Materials: The materials including lead(II) iodide (PbI_2), lead(II) bromide ($PbBr_2$), lead(II) chloride ($PbCl_2$), methylammonium bromide (MABr), [2-(3,6-dimethoxy-9H-carbazol-9-yl)ethyl]phosphonic acid (MeO-2PACz), phenyl-C_{61}-butyric acid methyl ester ($PC_{61}BM$), bathocuproine (BCP), and phenylpropylamine bromide (PPABr) were purchased from Xi'an Polymer Light Technology Corp. Cesium iodide (CsI), dimethylformamide (DMF), dimethyl sulfoxide (DMSO), chlorobenzene (CB), ethyl alcohol, acetone, and isopropanol (IPA) were purchased from Sigma–Aldrich. Formamidinium iodide (FAI) was purchased from Greatcell. All these materials were used directly without further purification.

Device Fabrication: The solar cell devices comprised ITO/MeO-2PACz/perovskite/$PC_{61}BM$/BCP/Cu. The formula for perovskite is $Cs_{0.05}FA_{0.875}MA_{0.075}PbI_{2.785}Br_{0.215}$. A slightly higher proportion (2.5 M%) of PbI_2 was added. In addition, $PbCl_2$ (1.0 M%) was used as an additive constituent in perovskite precursors to improve the device performance by reducing trap states and increasing charge collection. The ITO substrates were cleaned by sequentially sonicating in detergent solution, deionized water, ethyl alcohol, acetone, and IPA for 15 min each and putting in a drying oven for at least 3 h. Before preparation, the substrates were treated for 15 mins by UV. For the HTL, MeO-2PACz (35 µL solution of 3 mg mL^{-1}) in DMF was spin-coated at 3000 rpm for 30 s and annealed at 100 °C for 10 min. After cooling, DMF (35 µL) was spin-coated at 3000 rpm for 30 s and annealed at 100 °C for 10 min. The perovskite solution was prepared by mixing PbI_2 (615.24 mg), FAI (210.66 mg), $PbBr_2$ (35.97 mg), MABr (11.76 mg), and $PbCl_2$ (3.89 mg) in a mixture of a solution of DMF (0.85 mL) and DMSO (0.1 mL). As an additive into perovskite, PPABr (0.5 mg) would be added in the perovskite solution. CsI solution (50 µL of 363.6 mg mL^{-1} in DMSO) was mixed into the perovskite solution for at least 2 h with vibration before use. Perovskite solution (50 µL) was spin-coated at 1000 rpm for 5 s and at 4000 rpm for 21 s (both 2000 rpm ramp). At the 21st s in the whole setting, CB (120 µL) was uniformly deposited onto the substrate. Afterward, the ITO/PTAA/perovskite substrate was annealed at 100 °C for 7 min. For the upper surface modification, PPABr in IPA (30 µL of 1.0 mg mL^{-1}) was dynamically spun at 4000 rpm for 30 s and annealed at 100 °C for 5 min. The $PC_{61}BM$ (35 µL of 20 mg mL^{-1} in CB) was dynamically spun on the perovskite at 1000 rpm for 30 s and annealed at 100 °C for 3 min. BCP (35 µL of 1.0 mg mL^{-1} in IPA) was deposited at 4000 rpm. Last, a 100 nm-thick Cu electrode was thermally deposited.

Device and Film Characterization: The SEM tests were performed using a Zeiss (Merlin) scanning electron microscope at an accelerating voltage of 3.0 KV. AFM measurements were conducted with a Dimension Fastscan Atomic Force Microscope (Bruker Fastscan). The UPS and XPS measurements were done using an electron analyzer (ESCALAB 250Xi, Thermo Fisher Scientific) with a UV source ($h\upsilon = 21.2$ eV) for UPS and a monochromatic X ray source ($h\upsilon = 1486.7$ eV) for XPS in a main ultrahigh-vacuum chamber (base pressure, 1.0×10^{-10} mbar). A bias voltage of −5.0 V was applied to obtain the low energy secondary cutoff in the UPS measurement. The WF (Φ) was extracted from the SECO measurements of UPS spectra with bias. The total energy resolutions were determined as 50 meV (UPS) and 0.30 eV (XPS), respectively. The XRD patterns were obtained using a Bruker ECO D8 diffractometer. PL spectra were collected from a Princeton spectrometer (Acton, SpectraPro SP-2300) under an excitation of 400 nm (100 fs, 1 KHz). TRPL was conducted with a universal streak camera (Hamamatsu) with femtosecond laser as an optical excitation source. UV–vis absorption spectra were obtained from a UV–vis/NIR spectrophotometer (JASCO V-770EX). TA characterization was conducted using a HELIOS TA spectrometer. *J–V* curves were extracted under AM 1.5 G illumination through a solar simulator (Newport IEC/JIS/ASTM) equipped with a 450 W xenon lamp (spot size = 4×4 in.^{2}) and a Keithley 2400 source-meter. The intensity of the simulated solar light was standardized by a standard Si photodiode detector which was calibrated at the National Renewable Energy Laboratory. The Keithley 2400 source measure unit was used to record the device parameters.

Supporting Information

Supporting Information is available from the Wiley Online Library or from the author.

Acknowledgements

A.Z., H.G., and W.L. contributed equally to this work. The authors acknowledge the Science and Technology Development Fund from Macao SAR (Nos. FDCT-0044/2020/A1, 0082/2021/A2, 0010/2022/AMJ, and 006/2022/ALC), UM's research fund (Nos. MYRG2020-00151-IAPME,

MYRG2022-00241-IAPME, and MYRG-CRG2022-00009-FHS), the Wuyi University (EF38/IAPME-XGC/2022/WYU), the Natural Science Foundation of China (Nos. 61935017 and 62175268), and the Shenzhen-Hong Kong-Macao Science and Technology Innovation Project (Category C) (No. SGDX2020110309360100).

Conflict of Interest

The authors declare no conflict of interest.

Data Availability Statement

The data that support the findings of this study are available from the corresponding author upon reasonable request.

Keywords

organic ligand additives, perovskite solar cells, phenylpropylammonium bromide, synergistic passivation

Received: April 1, 2023
Revised: June 1, 2023
Published online:

[1] H. S. Jung, N. G. Park, *Small* **2015**, *11*, 10.
[2] P. Roya, N. K. Sinhaa, S. Tiwari, A. Kharea, *Sol. Energy* **2020**, *198*, 665.
[3] C. Liang, P. Li, H. Gu, Y. Zhang, F. Li, Y. Song, G. Shao, N. Mathews, G. Xing, *Sol. RRL* **2018**, *2*, 1700217.
[4] Y. Tu, J. Wu, G. Xu, X. Yang, R. Cai, Q. Gong, R. Zhu, W. Huang, *Adv. Mater.* **2021**, *33*, 2006545.
[5] National Renewable Energy Laboratory: Best Research-Cell Efficiency Chart, https://www.nrel.gov/pv/cell-efficiency.html (accessed: May 2023).
[6] C. Liang, H. Gu, J. Xia, S. Mei, P. Pang, N. Zhang, J. Guo, R. Guo, Y. Shen, S. Yang, Z. Wei, G. Shao, G. Xing, *Adv. Funct. Mater.* **2022**, *32*, 2108926.
[7] W. Hui, L. Chao, H. Lu, F. Xia, Q. Wei, Z. Su, T. Niu, L. Tao, B. Du, D. Li, Y. Wang, H. Dong, S. Zuo, B. Li, W. Shi, X. Ran, P. Li, H. Zhang, Z. Wu, C. Ran, L. Song, G. Xing, X. Gao, J. Zhang, Y. Xia, Y. Chen, W. Huang, *Science* **2021**, *371*, 1359.
[8] J. Park, J. Kim, H.-S. Yun, M. J. Paik, E. Noh, H. J. Mun, M. G. Kim, T. J. Shin, S. Il Seok, *Nature* **2023**, *616*, 724.
[9] T. Wu, Z. Qin, Y. Wang, Y. Wu, W. Chen, S. Zhang, M. Cai, S. Dai, J. Zhang, J. Liu, Z. Zhou, X. Liu, H. Segawa, H. Tan, Q. Tang, J. Fang, Y. Li, L. Ding, Z. Ning, Y. B. Qi, Y. Zhang, L. Han, *Nano-Micro Lett.* **2021**, *13*, 152.
[10] Z. Liu, L. Qiu, L. K. Ono, S. He, Z. Hu, M. Jiang, G. Tong, Z. Wu, Y. Jiang, D.-Y. Son, Y. Dang, S. Kazaoui, Y. Qi, *Nat. Energy* **2020**, *5*, 596.
[11] A. Extance, *Nature* **2019**, *570*, 429.
[12] Y. Hu, Z. He, X. Jia, S. Zhang, Y. Tang, J. Wang, M. Wang, G. Sun, G. Yuan, L. Han, *Small Methods* **2022**, *6*, 2101257.
[13] Z. Li, B. Li, X. Wu, S. A. Sheppard, S. Zhang, D. Gao, N. Long, Z. Zhu, *Science* **2022**, *376*, 416.
[14] W. Hui, Y. Yang, Q. Xu, H. Gu, S. Feng, Z. Su, M. Zhang, J. Wang, X. Li, J. Fang, F. Xia, Y. Xia, Y. Chen, X. Gao, W. Huang, *Adv. Mater.* **2020**, *32*, 1906374.
[15] W. Peng, K. Mao, F. Cai, H. Meng, Z. Zhu, T. Li, S. Yuan, Z. Xu, X. Feng, J. Xu, M. D. McGehee, J. Xu, *Science* **2023**, *379*, 6633.
[16] J. Xia, C. Liang, H. Gu, S. Mei, S. Li, N. Zhang, S. Chen, Y. Cai, G. Xing, *Energy Environ. Mater.* **2023**, *6*, e12296.
[17] P. Liu, N. Han, W. Wang, R. Ran, W. Zhou, Z. Shao, *Adv. Mater.* **2021**, *33*, 2002582.
[18] F. Huang, P. Siffalovic, B. Li, S. Yang, L. Zhang, P. Nadazdy, G. Cao, J. Tian, *Chem. Eng. J.* **2020**, *394*, 124959.
[19] F. Zheng, C. Zuo, M. Niu, C. Zhou, S. Bradley, C. Hall, W. Xu, X. Wen, X. Hao, M. Gao, T. A. Smith, K. P. Ghiggino, *ACS Appl. Mater. Interfaces* **2020**, *12*, 25980.
[20] F. Zhang, K. Zhu, *Adv. Energy Mater.* **2020**, *10*, 1902579.
[21] J. Xia, C. Liang, S. Mei, H. Gu, B. He, Z. Zhang, T. Liu, K. Wang, S. Wang, S. Chen, Y. Cai, G. Xing, *J. Mater. Chem. A* **2021**, *9*, 2919.
[22] M. E. Kamminga, H.-H. Fang, M. R. Filip, F. Giustino, J. Baas, G. R. Blake, M. A. Loi, T. T. M. Palstra, *Chem. Mater.* **2016**, *28*, 4554.
[23] B. E. Cohen, M. Wierzbowska, L. Etgar, *Sustainable Energy Fuels* **2017**, *1*, 1935.
[24] S. Song, S. J. Yang, W. Choi, H. Lee, W. Sung, C. Park, K. Cho, *Adv. Energy Mater.* **2020**, *10*, 2001759.
[25] J. Xi, I. Spanopoulos, K. Bang, J. Xu, H. Dong, Y. Yang, C. D. Malliakas, J. M. Hoffman, M. G. Kanatzidis, Z. Wu, *J. Am. Chem. Soc.* **2020**, *142*, 19705.
[26] T. Zhu, L. Shen, H. Chen, Y. Yang, L. Zheng, R. Chen, J. Zheng, J. Wang, X. Gong, *J. Mater. Chem. A* **2021**, *9*, 21910.
[27] Q. Jiang, Y. Zhao, X. Zhang, X. Yang, Y. Chen, Z. Chu, Q. Ye, X. Li, Z. Yin, J. You, *Nat. Photonics* **2019**, *13*, 460.
[28] A. Maqsood, Y. Li, J. Meng, Z. Qin, D. Song, B. Qiao, S. Zhao, Z. Xu, *ACS Appl. Energy Mater.* **2021**, *4*, 12411.
[29] Y. Liu, J. Duan, J. Zhang, S. Huang, W. Ou-Yang, Q. Bao, Z. Sun, X. Chen, *ACS Appl. Mater. Interfaces* **2019**, *12*, 771.
[30] S. Gharibzadeh, P. Fassl, I. M. Hossain, P. Rohrbeck, M. Frericks, M. Schmidt, T. Duong, M. R. Khan, T. Abzieher, B. A. Nejand, F. Schackmar, O. Almora, T. Feeney, R. Singh, D. Fuchs, U. Lemmer, J. P. Hofmann, S. A. L. Weber, U. W. Paetzold, *Energy Environ. Sci.* **2021**, *14*, 5875.
[31] W. Chen, Z. Gan, M. Green, B. Jia, X. Wen, *Small Methods* **2021**, *5*, 2000731.
[32] Q. Cheng, H. Xia, X. Li, B. Wang, Y. Li, X. Zhang, H. Zhang, Y. Zhang, H. Zhou, *Sol. RRL* **2021**, *6*, 2100805.
[33] C. Deng, J. Wu, Y. Du, Q. Chen, Z. Song, G. Li, X. Wang, J. Lin, W. Sun, M. Huang, Y. Huang, P. Gao, Z. Lan, *Small Methods* **2021**, *5*, 2101000.
[34] M. A. A. Kazemi, P. Raval, K. Cherednichekno, J. Chotard, A. Krishna, A. Demortiere, G. N. M. Reddy, F. Sauvage, *Small Methods* **2021**, *5*, 2000834.
[35] H. Gu, C. Liang, Y. Xia, Q. Wei, T. Liu, Y. Yang, W. Hui, H. Chen, T. Niu, L. Chao, Z. Wu, X. Xie, J. Qiu, G. Shao, X. Gao, G. Xing, Y. Chena, W. Huang, *Nano Energy* **2019**, *65*, 104050.
[36] Y. Shao, Z. Xiao, C. Bi, Y. Yuan, J. Huang, *Nat. Commun.* **2014**, *5*, 5784.
[37] C. Liang, H. Gu, Y. Xia, Z. Wang, X. Liu, J. Xia, S. Zuo, Y. Hu, X. Gao, W. Hui, L. Chao, T. Niu, M. Fang, H. Lu, H. Dong, H. Yu, S. Chen, X. Ran, L. Song, B. Li, J. Zhang, Y. Peng, G. Shao, J. Wang, Y. Chen, G. Xing, W. Huang, *Nat. Energy* **2021**, *6*, 38.
[38] B. Li, J. Deng, J. A. Smith, P. Caprioglio, K. Ji, D. Luo, J. D. McGettrick, K. I. Jayawardena, R. C. Kilbride, A. Ren, S. Hinder, J. Bi, T. Webb, I. Marko, X. Liu, Y. Xiang, J. Reding, H. Li, S. Du, D. G. Lidzey, S. D. Stranks, T. Watson, S. Sweeney, H. J. Snaith, S. R. P. Silva, W. Zhang, *Adv. Energy Mater.* **2022**, *12*, 2202868.
[39] A. Ullah, K. H. Park, H. D. Nguyen, Y. Siddique, S. F. A. Shah, H. Tran, S. Park, S. I. Lee, K.-K. Lee, C.-H. Han, K. Kim, S. Ahn, I. Jeong, Y. S. Park, S. Hong, *Adv. Energy Mater.* **2022**, *12*, 2103175.
[40] D. Yang, X. Zhang, K. Wang, C. Wu, R. Yang, Y. Hou, Y. Jiang, S. Liu, S. Priya, *Nano Lett.* **2019**, *19*, 3313.
[41] H. Gu, J. Xia, C. Liang, Y. Chen, W. Huang, G. Xing, *Nat. Rev. Mater.* **2023**, https://doi.org/10.1038/s41578-023-00560-2.

